Check for updates

Aluminum-rich reconstructed sapphire as a high-quality substrate for tungsten disulfide synthesis

Vesa-Matti Hiltunen, [ID] *[a] Marios Matheou, [ID] [b] Antonio Rossi, [ID] [a] Ben Richard Conran,[c] Kenneth Boh Khin Teo,[c] Stefano Dal Conte, [ID] [b] Armando Genco, [ID] [b] Giulio Cerullo, [ID] [b] Stiven Forti [ID] [a] and Camilla Coletti [ID] *[a]

2D transition-metal dichalcogenides have attracted significant attention due to their unique properties, which make them highly promising for a variety of applications ranging from quantum technologies, to electronic and photonic applications. In this context, developing scalable methods for high-quality synthesis is a major research priority, with chemical vapor deposition (CVD) emerging as the most promising approach. In this work, we reveal the critical role of substrate preparation in the CVD growth of tungsten disulfide (WS_2) on sapphire by comparing the aluminum-rich $(\sqrt{31} \times \sqrt{31})R \pm 9°$ reconstructed surface with a conventionally prepared one. We find that on average the reconstructed sapphire surface provides a significant 50% increase in crystal size and 125% increase in nucleation density. It also has a strong impact on the photoluminescence (PL) of WS_2 crystals, leading to quenching at the center while the edges exhibit intense red-shifted emission. Correlative Raman spectroscopy, atomic force microscopy (AFM), and Kelvin probe force microscopy (KPFM) analyses reveal that PL quenching in the center is due to a strong coupling between the Al-rich reconstructed sapphire and the WS_2 crystals, while the edges appear to be decoupled from the substrate, likely due to substrate degradation during the growth process. These findings highlight the importance of substrate reconstruction for tuning the morphology and optoelectronic properties of 2D materials.

Introduction

The quality of the growth substrate plays a critical role in the synthesis of 2D materials. While materials like graphene[1] and hexagonal boron nitride[2] are synthesized on metallic catalysts, which facilitate their growth by promoting precursor decomposition and crystalline alignment, transition metal dichalcogenides (TMDs) are typically synthesized on insulating substrates, such as SiO_2 or sapphire (α-Al_2O_3).[3] Metallic substrates are in most cases incompatible with the chemistries involved in the synthesis of typical TMDs, which are sulfur or selenium based, because of their chemical reactions with the chalcogen precursors at high temperatures. An exception to this is gold, which has been successfully used as a growth surface for MoS_2,[4–7]

WS_2[8–10] and WSe_2.[11] However, this approach can be quite expensive and difficult to scale up.

In this work, we use a simple hydrogen (H_2) annealing process to form an aluminum-rich $(\sqrt{31} \times \sqrt{31})R \pm 9°$ surface reconstruction on α-Al_2O_3 (0001) sapphire to facilitate the synthesis of WS_2. In this reconstruction, oxygen atoms are removed from the first few layers of the material, leaving an excess of aluminum (Al) atoms on the surface.[12–17] This surface, while not the same as bulk aluminum, has metallic properties, which should be beneficial for the synthesis of 2D materials. Previously, CVD growth of graphene on sapphire after H_2-annealing has been reported by our group,[18] and later by others.[19,20] A few studies have reported TMD growths on H_2-treated sapphire surfaces,[21–25] however, they did not verify the presence of $(\sqrt{31} \times \sqrt{31})R \pm 9°$ reconstruction induced by H_2 treatment, compare growth on reconstructed *versus* unreconstructed surfaces, nor provide detailed surface characterization. In this work we reveal the effect that such an Al-rich reconstructed surface has on WS_2 growth by investigating its properties with different spectroscopic and microscopic techniques and by performing a systematic comparison with WS_2 obtained on classically prepared sapphire substrates.

[a]Center for Nanotechnology Innovation @ NEST, Istituto Italiano di Tecnologia, Piazza San Silvestro 12, 56127 Pisa, Italy. E-mail: vesa.hiltunen@iit.it, Camilla.Coletti@iit.it
*[b]Dipartimento di Fisica, Politecnico di Milano, Piazza Leonardo Da Vinci 32, Milano, 20133, Italy*
[c]AIXTRON Ltd., Buckingway Business Park, Anderson Rd, Swavesey, Cambridge, CB24 4FQ, UK

Results and discussion

WS$_2$ crystals were grown on sapphire substrates treated under standard conditions, referred to in this work as *standard* sapphire, and on H$_2$-annealed substrates, referred to as *reconstructed* sapphire. As detailed in the Experimental section, *standard* sapphire indicates substrates subjected to solvent cleaning followed by high-temperature annealing in argon (Ar). To enable a clear comparison of the effect of the different growth substrates, WS$_2$ crystals were synthesized using tungsten trioxide (WO$_3$) and sulfur powder as precursors, without the use of any growth promoter. Full details of the growth conditions can be found in the Experimental section. Low energy electron diffraction (LEED) measurements were performed on the H$_2$ annealed substrates to verify the presence of the Al-rich reconstruction. While *standard* sapphire surfaces typically do not produce a measurable LEED pattern due to their insulating nature, Al-terminated surfaces can be characterized using LEED. As shown in Fig. 1a, the H$_2$-annealed sapphire exhibits a clear diffraction pattern corresponding to the $(\sqrt{31} \times \sqrt{31})R \pm 9°$ reconstruction,[18] confirming the Al termination of our growth substrate. Such reconstruction survives air exposure as confirmed by our observations (the LEED pattern in Fig. 1 was acquired after exposure to ambient conditions) and by previous literature reports.[18]
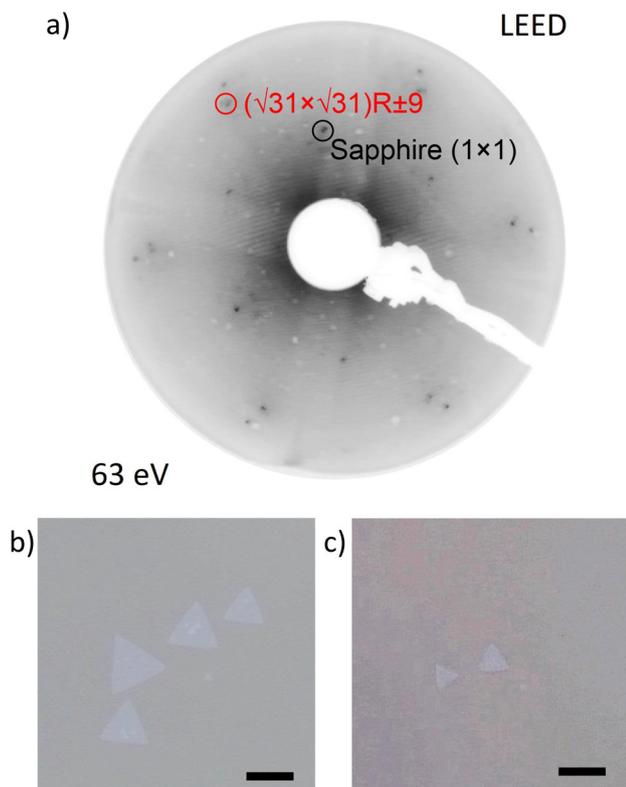
When WS$_2$ is grown following the same process on *reconstructed* and *standard* sapphire surfaces, there are clear differences in the results. A visual comparison of WS$_2$ growth on these substrates is presented in Fig. 1b and c, showing that on the *reconstructed* substrate the grown crystals are higher in number and larger in size. A comparison of the average WS$_2$ crystal size and density on these two surfaces calculated from several growth batches is presented in Table 1. Representative images of the samples used for these calculations are presented in SI Fig. S1. The crystals are, on average, 50% larger and 125% denser on *reconstructed* sapphire than on *standard* sapphire. In other words, Al-rich reconstruction clearly increases both the lateral size of the WS$_2$ crystals and the nucleation density, which is an indication of the increased catalytic activity of the Al-rich surface.

In order to study in depth the properties of the WS$_2$ crystals, we performed photoluminescence (PL) spectroscopy measurements. The PL intensity and position maps of a typical WS$_2$ crystal grown on *standard* sapphire are presented in Fig. 2a and b. The intensity is very consistent throughout the entire flake, except for the slight decrease at the nucleation point at the very center of the flake. The peak positions follow the same trend as the intensity, with only clear variations occurring at the nucleation point and at the very edges of the crystal. These variations are evident in the two representative spectra reported in Fig. 2c, where the spectrum from the crystal edge exhibits a noticeably more prominent low-energy tail compared to that from the center. The low-energy tail and the slight red-shift of the PL peak can be explained by a higher density of sulfur defects at the edges, which have been observed before for TMD materials synthesized by CVD.[26–29] Fig. 2d and e show the same plots for a WS$_2$ crystal grown on *reconstructed* sapphire. In particular, the intensity map shows a drastic difference, with the PL significantly reduced at the center and the highest PL intensity located at the very edges of the crystal. High intensity edges are a consistent feature of the crystals grown on *reconstructed* sapphire, which can also be seen from the large-scale PL map in SI Fig. S2. In all measurements reported in Fig. 2, the laser spot size is less than 1 μm and the step size is 0.5 μm, indicating that the width of the edge ribbon is in the range of 0.5–1 μm. The map in Fig. 2e shows that at the edges there is also a redshift of the PL posi-

Fig. 1 H$_2$-annealing of sapphire. (a) Diffraction pattern of H$_2$-annealed sapphire measured by LEED at 63 eV, showing the $(\sqrt{31} \times \sqrt{31})R \pm 9°$ surface reconstruction. (b) WS$_2$ crystals grown on H$_2$-annealed sapphire. (c) WS$_2$ grown on *standard* sapphire. The scale bars are 20 μm.

Table 1 Average crystal size and density values calculated from five sample batches. The error in crystal sizes is the standard deviation and in density it is calculated from pixel size calibration error

	Standard sapphire		Reconstructed sapphire	
	Crystal size (μm)	Density (1/mm²)	Crystal size (μm)	Density (1/mm²)
Batch 1	14.3 ± 5.7	72 ± 2	23.8 ± 8.9	213 ± 5
Batch 2	8.0 ± 2.3	45 ± 1	22.0 ± 8.5	187 ± 4
Batch 3	16.8 ± 7.4	107 ± 3	22.5 ± 8.4	105 ± 3
Batch 4	23.0 ± 10.0	51 ± 1	27.4 ± 11.6	72 ± 2
Batch 5	12.4 ± 4.7	18 ± 1	15.7 ± 7.3	81 ± 2
Average	14.9 ± 6.0	59 ± 1	22.3 ± 9.0	132 ± 3
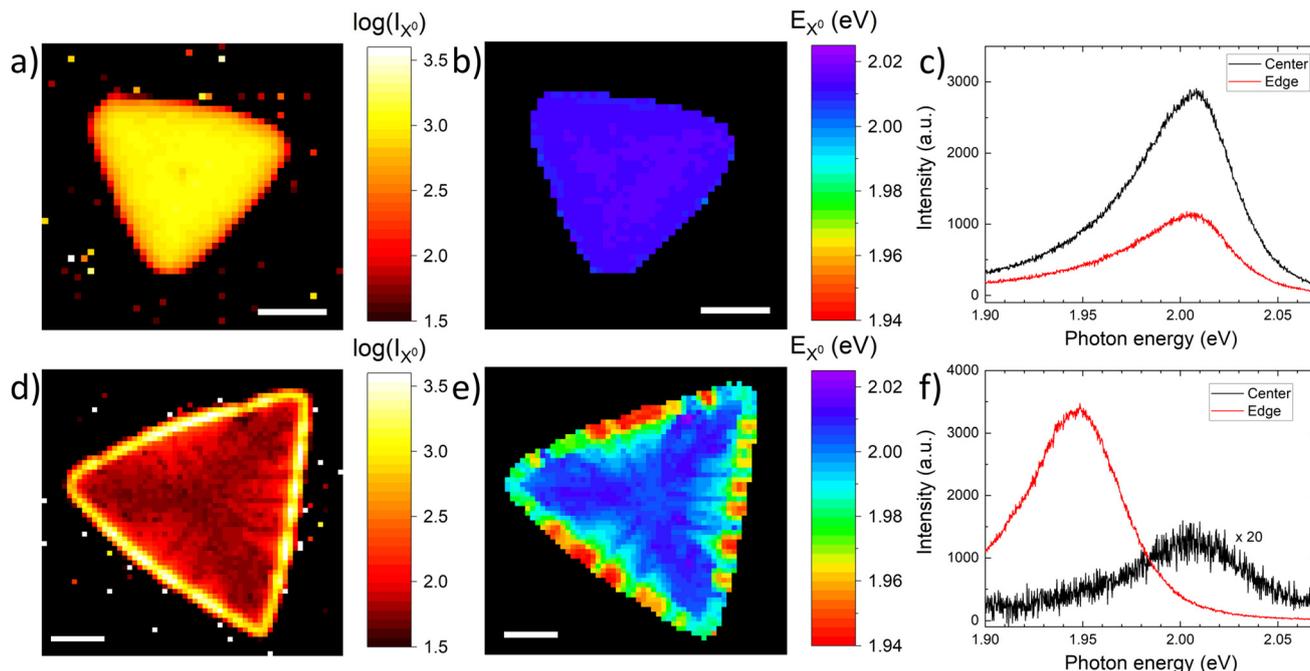
Fig. 2 Different behavior of WS$_2$ crystals grown on *standard* and *reconstructed* sapphire. (a) PL intensity, (b) peak energy maps and (c) exemplary spectra of WS$_2$ grown on *standard* sapphire. (d), (e) and (f) are the same for *reconstructed* sapphire, respectively. The intensity of the spectrum shown in (f), collected from the center of the crystal, has been multiplied by a factor of 20 to enhance visibility. All scale bars are 5 μm.

tion. The representative spectra in Fig. 2f, taken from the center and edge of the crystal, clearly show the drastic difference between the two. Furthermore, both intensity and peak energy maps acquired on *reconstructed* sapphire evidence a distinct 3-fold symmetric PL inhomogeneity in the inner part of the crystal, which is due to strain variations, as we demonstrate later in the manuscript. The decreased overall PL intensity and red-shift of the PL peak position of the crystals in the *reconstructed* sapphire can be rationalized by the interplay between substrate coupling and defectiveness. The strong electronic coupling at the crystal centers enables charge transfer to the metallic Al-terminated surface, quenching the emission. This restores radiative efficiency while defect-related trionic and excitonic recombination produces a redshifted emission. A similar correlation between interfacial decoupling and enhanced PL was reported by Zhang *et al.*,[30] who observed an approximate 0.37 nm increase in WS$_2$–sapphire separation at the edges. Comparable edge-localized excitonic red shifts linked to sulfur vacancies or trion formation were also observed by Carozo *et al.*,[28] Gu *et al.*,[31] and Kastl *et al.*[29]

A possible explanation for the different behavior between the center and the edge of the crystals is differences in strain[32–37] and charge doping[38–40] between these regions. These changes can also be measured using Raman spectroscopy; therefore, cross-referencing PL data with Raman data can give us a good idea of whether the differences are indeed caused by strain and doping. PL and Raman spectroscopy data measured from the same crystal and presented in SI Fig. S3, indicate that there are correlations between the positions of

the E' and A_1' Raman peaks and the observed changes in the PL spectra. There also appears to be a difference in the Raman peak positions between the WS$_2$ crystals grown on the two substrates, which is shown in SI Fig. S4. To study this matter further, we measured Raman spectral maps from several different crystals grown on *reconstructed* sapphire and extracted the Raman peak position data separately from edge regions where PL intensity is high and dim central regions. To compare crystals grown on different substrates, we performed the same analysis on crystals grown on *standard* sapphire by separating the data from the 1 μm wide edge region and the center. The results of this analysis are presented in the correlation plots reported in Fig. 3. The data from WS$_2$ grown on *reconstructed* sapphire in Fig. 3a shows that the central regions of the crystals are strained and some of them slightly p-type doped. At the edges, the stress is relaxed and the doping decreased, some of the crystals even becoming slightly n-type doped. With the flakes on a *standard* sapphire substrate in Fig. 3b there is only a slight release of strain toward the edges of the crystals, while doping does not change. However, in Fig. 3a the differences among individual crystals are larger than a shift within any crystal, and some of the edge regions remain more strained than the central regions of other crystals. Therefore, it is safe to say that, while strain and doping might be contributing factors, differences in PL are not caused by them.

The quenched PL intensity in the center and red-shifted edge regions shown in Fig. 2 resembles the differences between sulfur- and tungsten-deficient WS$_2$ regions, which
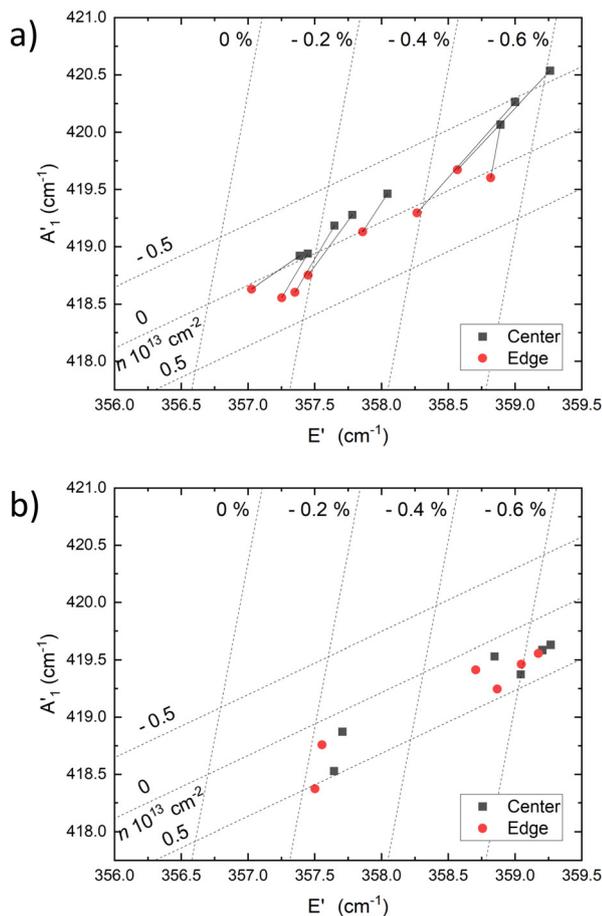
Fig. 3 A comparison of E' and A_1' Raman positions at the center and the edge of the WS$_2$ flakes. (a) WS$_2$ grown on *reconstructed* sapphire and (b) WS$_2$ grown on *standard* sapphire. Connecting lines between data point in (a) indicate data from the same crystal. The horizontal dotted lines with a slope of 0.55 indicate constant doping level and vertical dotted lines with a slope of 6.16 constant strain. The point with neutral doping and strain is $\omega(E') = 356.7$ cm^{-1} and $\omega(A_1') = 418.5$ cm^{-1}. The slopes and the neutrality point are based on previous work by Lee *et al.*[36]

have been described in numerous previous works.[41–45] However, we do not see the same Raman behavior reported in these works, such as differences in the Raman peak intensities between the two regions (SI Fig. S3). Additionally, in all of the cases where W deficient regions are present, the crystals have been grown in a particular way with sodium promoter under W deficient conditions, which leads to hexagonal crystal growth. If our results were to be explained by differences in the concentrations of W and S defects, this would indicate a sudden rush of W species to the growing crystals at the very end of the growth process, forming only a thin sulfur-deficient sliver. However, this is not feasible under the growth conditions used here and is not seen with crystals grown on *standard* sapphire, which should be expected since the samples were grown in the same batch and sitting next to each other.

To better understand the PL behavior observed at the WS$_2$ crystal edges on *reconstructed* sapphire, we performed atomic

force microscopy (AFM) and Kelvin probe force microscopy (KPFM) measurements. KPFM measurements have previously been used to assess the defectiveness of WS$_2$ crystals.[29,46] A representative AFM scan of an edge region of WS$_2$ grown on *reconstructed* sapphire is reported in Fig. 4a and shows that there is no damage or impurities visible on this scale. On the other hand, the surface potential image in Fig. 4b and the line profile in Fig. 4c show a decreased surface potential value at the very edge of the crystal. The potential gradually becomes the same as in the WS$_2$ center within a distance of about 1 µm from the crystal edge, which is a perfect match to the width of the high-intensity edge in Fig. 2. The difference in surface potential is approximately 400 mV. Interestingly, Wang *et al.*[46] measured a similar potential difference with the same type of microscope setup from two WS$_2$ regions with different defect densities. The spatial correlation of the decrease in surface potential with the red-shift of the PL peak position gives additional evidence that the red-shift is caused by defect-rich domains, as mentioned above.

Examination of the high-resolution AFM images in Fig. 4d–f reveals detailed structural characteristics at the edge of the crystal. The profile plot in Fig. 4e shows that the WS$_2$ height is about 700 pm, in agreement with what is reported in the literature. At the edge of the WS$_2$ crystal, in Fig. 4d, numerous nanoscale holes are observed. Fig. 4f taken moving away (about 1 µm) from the very edge of the crystal shows that the density of holes decreases, while small islands protruding above the base level become more prevalent. Both the pits and the islands have approximately the same 200 pm height difference compared to their base levels, which corresponds to the height of a single O–Al–O trilayer.[47,48] Such pits and an overall increase in sapphire roughness are distinctive both at the WS$_2$ edges and outside the flakes, and appear only after the growth process (see SI Fig. S5). In the inner part of the WS$_2$ flake even the island features disappear, and the surface is much smoother compared to the edge. It should be noted that such an uneven morphology is not observed on *standard* sapphire and is therefore something distinctive of growths on *reconstructed* sapphire.

The measurements described above give a clear indication that the *reconstructed* sapphire substrate has a strong effect on the results. Therefore, next we studied the effect of the substrate on the PL properties of the WS$_2$ crystals by doing PL measurements on crystals transferred onto SiO$_2$/Si substrates. For details of the transfer process, see the Experimental section. Fig. 5 presents a comparison of PL intensity maps measured from the same crystal before and after transfer. Before transfer in Fig. 5a, the crystal exhibits the same high intensity edge luminescence described in Fig. 2. This is contrasted by the after transfer map in Fig. 5, which shows an evenly high-intensity PL throughout the entire crystal. This comparison provides the clearest possible evidence that the PL behavior seen from the crystals on *reconstructed* sapphire is not caused by differences in intrinsic properties within the crystals, but by interaction with the substrate.

To further study the effect of the substrate on the PL properties of the WS$_2$ crystals, we performed hyperspectral PL
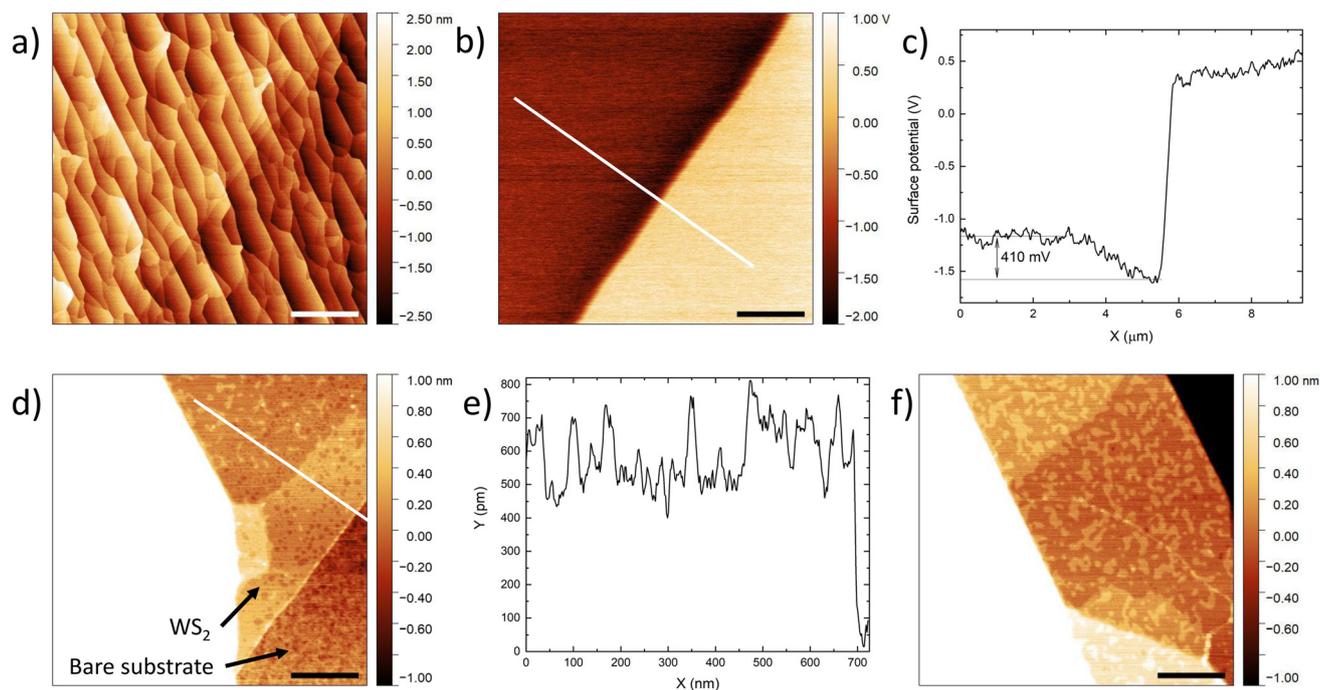
Fig. 4 AFM and KPFM measurements of WS_2 on *reconstructed* sapphire. (a) Height image and (b) surface potential image from a WS_2 crystal edge. (c) A line profile, which position is indicated by the white line in (b). (d) High resolution height image from the crystal edge and (e) line profile, taken along the white line in (d). (f) High resolution height image measured moving towards the central region of the crystal. White regions in d and f and black region in f are due to sapphire terrace edge step being larger (>2 nm) than color scale, which is meant to showcase the small (200 pm) holes and protruding island features. Scale bars are 2 μm for (a) and (b) and 200 nm for (d) and (f).
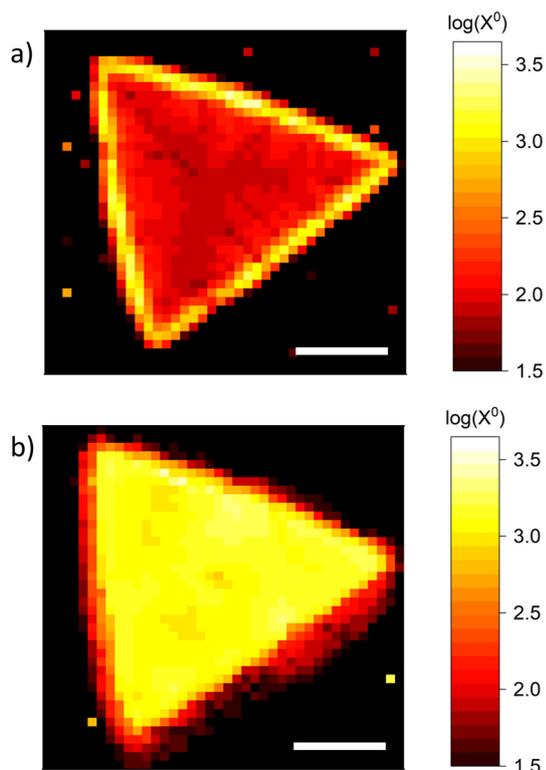
**Fig. 5** PL intensity maps of the same WS_2 crystal (a) before transfer from Al-rich *reconstructed* sapphire surface and (b) after transfer onto SiO_2/Si surface. The scale bars are 5 μm.

measurements of the crystals grown on *reconstructed* sapphire and after transfer to the SiO_2/Si surface, and performed statistical analysis of the spectral data. The results of these measurements are presented in Fig. 6. The crystal before transfer in Fig. 6a exhibits much more variations in the peak position of the neutral exciton compared to the transferred flake in Fig. 6d. The threefold symmetric blue-shifted lines in Fig. 6a and d going from the centers to the tips of the triangle crystals are tungsten deficient lines that are mechanistically known to appear when WS_2 is synthesized with CVD.[29,41] This can also be seen when comparing histograms derived from the maps in Fig. 6b and e, where the distribution is very broad before transfer and decreases significantly after transfer, as can be seen from the standard deviation values. This is a further indication that the main PL features described earlier are due to the interaction with the substrate since after the transfer the substrate is electrostatically uniform across the whole crystal. Furthermore, the intensity histograms in Fig. 6c and f clearly show that the mean PL intensity increases after transfer, which is the result of the removal of the quenching effect when crystals are transferred from the Al-terminated *reconstructed* sapphire to the SiO_2 surface.

These observations provide valuable insight into the growth dynamics of WS_2 on *reconstructed* sapphire. The CVD synthesis of WS_2 from solid precursors is characterized by rapid reaction kinetics between tungsten and sulfur.[49–51] We propose that the bulk of WS_2 formation occurs early in the process on the
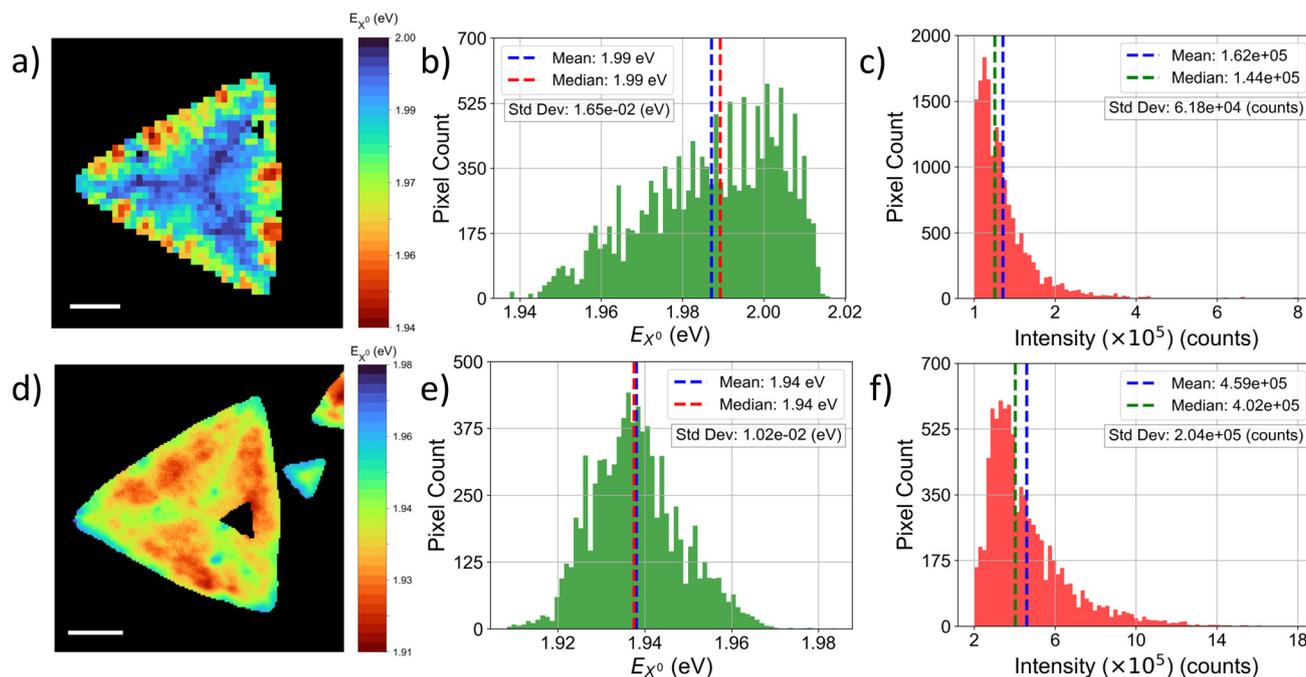
Fig. 6 Comparison of hyperspectral measurements of WS$_2$ crystals grown on reconstructed sapphire and those transferred on 90 nm SiO$_2$/Si substrate. (a) Map of neutral exciton peak position of crystals on reconstructed sapphire, (b), (c) histograms of peak position and intensity distribution for measured area with crystals on reconstructed sapphire, (d), (e), and (f) are the same for transferred crystals. All scale bars are 5 μm.

catalytically active, Al-rich *reconstructed* sapphire surface. However, during the final stages of growth and subsequent cool-down, the prolonged exposure of this surface to a sulfur-rich environment likely leads to its partial sulfurization, resulting in morphological inhomogeneities. As a consequence, the lateral expansion of the last micrometer of the WS$_2$ crystals likely proceeds on a chemically altered substrate, where weakened interfacial coupling at the edges reduces PL quenching and enhances edge emission.[26–29] Indeed, surface modification during growth is confirmed by LEED analysis performed on a reconstructed sapphire substrate after a prolonged WS$_2$ synthesis (15 min), which reveals a (1×1) surface termination, indicating the loss of the initial $(\sqrt{31} \times \sqrt{31})R \pm 9°$ reconstruction (see SI Fig. S6). Also, one should note that aluminum sulfide hydrolyzes in air, which might further enhance the decoupling at the crystal edges during exposure of the sample to ambient conditions. Furthermore, as supported by the KPFM analysis – and plausibly due to the local variations in substrate composition during growth – the edges of the crystals exhibit a higher density of defects compared to their central regions. This increased defectiveness is expected to enhance trion and biexciton recombination, contributing to the observed red-shift in the PL signal.[26,28,29,31] The simultaneous occurrence of reduced interfacial coupling and higher defect density at the crystal periphery offers a coherent explanation for the distinct PL behavior observed at the edges.

Finally, confirmation that the PL quenching observed in the center of the crystals is to be assigned to the strong coupling arising during growth between WS$_2$ and the metallic-like

reconstructed sapphire is supported by PL maps acquired after transferring these WS$_2$ crystals onto various substrates (*i.e.*, SiO$_2$, fresh *reconstructed* sapphire and silicon nitride (SiN))(see SI Fig. S7). In all cases, the PL intensity is uniform across the crystals, with no apparent difference between the edge and the center, as expected if the emission is primarily influenced by the interaction with the substrate. Notably, when transferring WS$_2$ on a fresh *reconstructed* sapphire substrate the PL intensity is lower than on SiO$_2$ or SiN, as can be expected when placing WS$_2$ on a substrate with metallic character. However, the fresh *reconstructed* sapphire surface is homogeneous, since none of it has reacted with sulfur, and thus the PL measured from the crystal transferred onto it is also homogeneous. On the other hand, the coupling between the WS$_2$ crystal and the fresh *reconstructed* sapphire surface cannot be assumed to be high, since they have not undergone a high-temperature process together. In order to reproduce the PL behavior on a new substrate, both high substrate/TMD coupling and substrate degradation at the edges are needed. This stronger adhesion is further evidenced by the transfer process: while crystals grown on *standard* sapphire readily detach in deionized water, those grown on *reconstructed* sapphire require a more effective NaOH treatment, in line with a stronger interfacial interaction developed during synthesis.

Conclusions

In conclusion, we demonstrate that sapphire substrates with Al-rich surface reconstruction significantly enhance the CVD

growth of WS_2, resulting in larger crystal domains and higher nucleation density compared to conventionally prepared substrates. Considering TMDs with similar chemistry (such as MoS_2 or WSe_2), one could anticipate a comparable trend when employing *reconstructed* surfaces for their synthesis, provided that the growth parameters are properly optimized. The reported results highlight the critical role of pre-growth substrate engineering in optimizing the morphology and yield of 2D semiconductors. Beyond structural improvements, the reconstructed surface also has a marked influence on the optical response of the grown crystals, notably inducing photoluminescence quenching in most of the crystal with the exception of the edges. Correlative analyses point to a strong electronic coupling at the WS_2–sapphire interface as the origin of this effect, with weakened coupling at the crystal periphery caused by substrate degradation during growth. Such substrate degradation takes place at the very edges (about 1 μm) of the WS_2 crystals, and it is likely the reason for increased defectiveness in this peripheral region. These findings establish Al-rich reconstructed sapphire not only as a growth-enhancing platform for WS_2, but also as a means to modulate interfacial properties, offering new opportunities for the controlled integration of 2D semiconductors into advanced optoelectronic and photonic architectures.

Experimental

Sapphire preparation

An AIXTRON cold-wall MOCVD reactor (CCS2D) was used for high-temperature annealing of sapphire substrates. To form the $(\sqrt{31} \times \sqrt{31})R \pm 9°$ surface reconstruction, sapphire substrates (*C*-plane (0001) 0.2° off *M*-axis, 2-inch wafers, Silian optoelectronics) were heated >1200 °C temperature.[18] The substrates were kept at processing temperature for 10 minutes under 40 slm H_2 gas flow at 150 mbar pressure.

For comparison purposes, sapphire substrates prepared in a *standard* method (*C*-plane (0001) 0.2° off *M*-axis, Silian optoelectronics) were annealed before growth at 1000 °C temperature for 1 hour under 800 sccm Ar flow at 5 mbar pressure.

CVD details

WS_2 crystals were synthesized by Chemical Vapor Deposition (CVD) from powder WO_3 (99.995%, Sigma-Aldrich) and sulfur (99.998%, Sigma-Aldrich) sources on sapphire substrates prepared as described above. Growths on both sapphire substrates were conducted in exactly the same way. The sapphire growth substrates were placed directly above the WO_3 precursor powder with sapphire spacers. The distance between the precursor powder and the growth substrate was controlled with the thickness of the spacers. The samples and precursors were then loaded into a quartz tube furnace (Carbolite Gero TS1 12/200/600) for synthesis. The atmosphere of the reaction chamber was replaced with Ar by performing three consecutive pump–purge cycles to ensure an inert environment prior to deposition. The chamber was filled to about 950 mbar

pressure and heated to a temperature of 930 °C with a ramp of 10 °C min^{-1} under 125 sccm of Ar flow. Right before reaching the growth temperature, the pressure was lowered to 100 mbar and both pumping and injection gas flow was stopped, so that the growth was carried out under quasi-static conditions, similar to what was previously reported by Xia *et al.*[52] The duration of the growth step was 15 min and once the time had elapsed, the chamber was let to naturally cool under 125 sccm Ar flow.

Transfer

Before transfer, the samples were spin coated with PMMA support at 4000 rpm for 60 seconds and baked at 90 °C for 2 minutes, followed by placement of the PDMS frame on the PMMA. The support polymers with the WS_2 crystals were delaminated by immersing the sample in deionized (DI) water or 1 M NaOH. Then, the entire stack was rinsed in DI water and let to dry in air before placing the stack on the target substrate. The samples were heated to 100 °C to detach the PDMS frame and the PMMA was dissolved in acetone, followed by a rinse in isopropyl alcohol and drying with a nitrogen gun.

Optical microscopy

Optical microscope images were taken with Zeiss Axioscope 7 equipped with Axiocam 208 color camera. The crystal sizes and densities were calculated from the optical images using Gwyddion 2.66 software by applying a threshold mask and calculating the statistics using the grain analysis tools of the software.

LEED

Low-energy electron diffraction (LEED) measurements were carried out at room temperature at a base pressure of 8^{-10} mbar with a Specs GmbH ErLEED 150 instrument. The sample was mounted on a VacGen Ltd transfer arm, with 4 movable axes.

Raman and photoluminescence spectroscopy

Spectroscopic characterization was performed using a Renishaw inVia Raman microscope setup. Raman spectra were collected using a 473 nm laser, a 2400 1/mm diffraction grating and a 100 × 0.85 NA objective, yielding approximately 0.68 μm spot size. Photoluminescence measurements were performed with the same setup, except that the laser and grating used were 532 nm and 1800 1/mm, respectively, yielding an approximately 0.77 μm spot size.

Fourier transform hyperspectral photoluminescence measurements

Hyperspectral photoluminescence (PL) measurements were performed using a commercial *epi*-illumination optical microscope (Leica DMRBE) that was customized to enable fiber coupling.[53,54] The standard eyepiece was replaced with a Translated Wedge-based Identical Pulses eNcoding System (TWINS) common-path birefringent interferometer,[55] following the implementation described by Trovatello *et al.*[56] Above

the interferometer an EMCCD camera (Andor LucaEM R, 1004 1002 pixels, 8 μm pixel size, 14-bit depth) was mounted to capture the interferometric signal. For excitation, a green diode laser (λ = 532 nm) with a power density of approximately 10 μW μm^{-2}, delivered through a 300 μm core diameter multimode fiber, was used. This configuration produced an illumination spot size of approximately 98.4 μm on the sample surface. A filter cube within the microscope directed the excitation light toward the sample and transmitted the emitted or reflected light toward the detection path. Light from the sample was collected using a 50× HC PL FLUOTAR objective lens with a numerical aperture (N.A.) of 0.8. For hyperspectral data acquisition, the birefringent wedges of the TWINS interferometer were translated over a ±1 mm range centered around the zero-path delay position, with a step size of 5 μm. This resulted in a total of 400 steps. The Fourier transform of the temporal interferometric data to generate the spectral hypercube was performed on a standard commercial PC (Intel i7 CPU, 16 GB RAM), requiring only a few tens of seconds.

Statistical analysis

A decomposition method based on the Turbo colorscale—a 256-color gradient, was employed to convert the RGB pixel values into the corresponding numerical indices ranging from 0 to 1. Each color along the Turbo scale represents a unique scalar value, enabling the transformation of RGB color information into a one-dimensional numerical format. For both the wavelength and intensity maps, each pixel was assigned a scalar value by matching its RGB color to the closest entry in the Turbo colormap. This allowed for a quantitative analysis of color-coded image data. To remove background contributions, a filtering step was applied to the intensity maps. Pixels with values below a defined intensity threshold were excluded from further analysis, ensuring that only signal-relevant regions were retained.

AFM and KPFM

Atomic Force Microscopy and Kelvin Probe Force Microscopy measurements were performed with Bruker Dimension Icon tool using PFQNE-AL probes with a nominal spring constant of 0.8 N m^{-1} and a nominal tip radius of 5 nm. All measurements were performed in ambient air.

Author contributions

V.-M. H. performed Ar annealing of the sapphire substrates, WS$_2$ growth and Raman spectroscopy, PL spectroscopy, optical microscopy, AFM and KPFM measurements and analyses. B. R. C. performed the H$_2$ annealing of the sapphire substrates. S. F. performed the LEED measurements and analysis. M. M. performed the hyperspectral PL measurements and analysis. V.-M. H., M. M., A. R., A. G., S. F. and C. C. wrote the original manuscript. K. B. K. T., S. D. C., A. G., G. C. and C. C. supervised the work. All authors reviewed the manuscript.

Conflicts of interest

There are no conflicts of interest to declare.

Data availability

The data supporting this article have been included as part of the supplementary information (SI).

Supplementary information: example images from samples based on grain statistics calculations, large-scale optical microscope and photoluminescence images, a collage of Raman and PL spectroscopy map images, additional Raman data, additional AFM images and PL map images before *vs.* after transfer onto various substrates. See DOI: https://doi.org/10.1039/d5nr03765d.

Acknowledgements

References

1 X. Li, W. Cai, J. An, S. Kim, J. Nah, D. Yang, R. Piner, A. Velamakanni, I. Jung, E. Tutuc, S. K. Banerjee, L. Colombo and R. S. Ruoff, *Science*, 2009, **324**, 1312–1314.

2 Y. Wang, C. Zhao, X. Gao, L. Zheng, J. Qian, X. Gao, J. Li, J. Tang, C. Tan, J. Wang, X. Zhu, J. Guo, Z. Liu, F. Ding and H. Peng, *Nat. Mater.*, 2024, **23**, 1495–1501.

3 L. Li, Q. Wang, F. Wu, Q. Xu, J. Tian, Z. Huang, Q. Wang, X. Zhao, Q. Zhang, Q. Fan, X. Li, Y. Peng, Y. Zhang, K. Ji, A. Zhi, H. Sun, M. Zhu, J. Zhu, N. Lu, Y. Lu, S. Wang, X. Bai, Y. Xu, W. Yang, N. Li, D. Shi, L. Xian, K. Liu, L. Du and G. Zhang, *Nat. Commun.*, 2024, **15**, 1825.

4 J. Shi, D. Ma, G.-F. Han, Y. Zhang, Q. Ji, T. Gao, J. Sun, X. Song, C. Li, Y. Zhang, X.-Y. Lang, Y. Zhang and Z. Liu, *ACS Nano*, 2014, **8**, 10196–10204.

5 J. Shi, Y. Yang, Y. Zhang, D. Ma, W. Wei, Q. Ji, Y. Zhang, X. Song, T. Gao, C. Li, X. Bao, Z. Liu, Q. Fu and Y. Zhang, *Adv. Funct. Mater.*, 2015, **25**, 842–849.

6 P. Yang, S. Zhang, S. Pan, B. Tang, Y. Liang, X. Zhao, Z. Zhang, J. Shi, Y. Huan, Y. Shi, S. J. Pennycook, Z. Ren, G. Zhang, Q. Chen, X. Zou, Z. Liu and Y. Zhang, *ACS Nano*, 2020, **14**, 5036–5045.

7 H. Lei, W. Wei, Z. Gong, H. Li and Y. Cui, *ACS Appl. Nano Mater.*, 2024, **7**, 3931–3938.

8 S. J. Yun, S. H. Chae, H. Kim, J. C. Park, J.-H. Park, G. H. Han, J. S. Lee, S. M. Kim, H. M. Oh, J. Seok, M. S. Jeong, K. K. Kim and Y. H. Lee, *ACS Nano*, 2015, **9**, 5510–5519.

9 Y. Gao, Z. Liu, D.-M. Sun, L. Huang, L.-P. Ma, L.-C. Yin, T. Ma, Z. Zhang, X.-L. Ma, L.-M. Peng, H.-M. Cheng and W. Ren, *Nat. Commun.*, 2015, **6**, 8569.

10 J. Wang, Y. Lu, W. Quan, J. Hu, P. Yang, G. Song, J. Fu, Y. Peng, L. Tong, Q. Ji and Y. Zhang, *ACS Nano*, 2024, **18**, 26359–26368.

11 S. J. Yun, S. M. Kim, K. K. Kim and Y. H. Lee, *Curr. Appl. Phys.*, 2016, **16**, 1216–1222.

12 J. V. Lauritsen, M. C. R. Jensen, K. Venkataramani, B. Hinnemann, S. Helveg, B. S. Clausen and F. Besenbacher, *Phys. Rev. Lett.*, 2009, **103**, 076103.

13 M. Gautier, J. Duraud, L. Pham Van and M. Guittet, *Surf. Sci.*, 1991, **250**, 71–80.

14 G. Renaud, B. Villette, I. Vilfan and A. Bourret, *Phys. Rev. Lett.*, 1994, **73**, 1825–1828.

15 E. A. A. Jarvis and E. A. Carter, *J. Phys. Chem. B*, 2001, **105**, 4045–4052.

16 C. Barth and R. Michael, *Nature*, 2001, **414**, 54–57.

17 J. I. Hütner, A. Conti, D. Kugler, F. Mittendorfer, G. Kresse, M. Schmid, U. Diebold and J. Balajka, *Science*, 2024, **385**, 1241–1244.

18 N. Mishra, S. Forti, F. Fabbri, L. Martini, C. McAleese, B. R. Conran, P. R. Whelan, A. Shivayogimath, B. S. Jessen, L. Buß, J. Falta, I. Aliaj, S. Roddaro, J. I. Flege, P. Bøggild, K. B. K. Teo and C. Coletti, *Small*, 2019, **15**, 1904906.

19 H. Wördenweber, S. Karthäuser, A. Grundmann, Z. Wang, S. Aussen, H. Kalisch, A. Vescan, M. Heuken, R. Waser and S. Hoffmann-Eifert, *Sci. Rep.*, 2022, **12**, 18743.

20 Y. Kawai, T. Nakao, T. Oda, N. Ohtani and H. Hibino, *Jpn. J. Appl. Phys.*, 2023, **62**, 085503.

21 M. Marx, A. Grundmann, Y.-R. Lin, D. Andrzejewski, T. Kümmell, G. Bacher, M. Heuken, H. Kalisch and A. Vescan, *J. Electron. Mater.*, 2018, **47**, 910–916.

22 S. Pace, M. Ferrera, D. Convertino, G. Piccinini, M. Magnozzi, N. Mishra, S. Forti, F. Bisio, M. Canepa, F. Fabbri and C. Coletti, *J. Phys. Mater.*, 2021, **4**, 024002.

23 H. Tang, S. Pasko, S. Krotkus, T. Anders, C. Wockel, J. Mischke, X. Wang, B. Conran, C. McAleese, K. Teo, S. Banerjee, H. M. Silva, P. Morin, I. Asselberghs, A. Ghiami, A. Grundmann, S. Tang, H. Fiadziushkin, H. Kalisch, A. Vescan, S. El Kazzi, A. Marty, D. Dosenovic, H. Okuno, L. Le Van-Jodin and M. Heuken, *J. Cryst. Growth*, 2023, **608**, 127111.

24 S. Tang, A. Grundmann, H. Fiadziushkin, Z. Wang, S. Hoffmann-Eifert, A. Ghiami, A. Debald, M. Heuken, A. Vescan and H. Kalisch, *Cryst. Growth Des.*, 2023, **23**, 1547–1558.

25 A. Ghiami, H. Fiadziushkin, T. Sun, S. Tang, Y. Wang, E. Mayer, J. M. Schneider, A. Piacentini, M. C. Lemme, M. Heuken, H. Kalisch and A. Vescan, *ACS Appl. Electron. Mater.*, 2025, **7**, 2394–2403.

26 H. R. Gutiérrez, N. Perea-López, A. L. Elías, A. Berkdemir, B. Wang, R. Lv, F. López-Urías, V. H. Crespi, H. Terrones and M. Terrones, *Nano Lett.*, 2013, **13**, 3447–3454.

27 W. Bao, N. J. Borys, C. Ko, J. Suh, W. Fan, A. Thron, Y. Zhang, A. Buyanin, J. Zhang, S. Cabrini, P. D. Ashby, A. Weber-Bargioni, S. Tongay, S. Aloni, D. F. Ogletree, J. Wu, M. B. Salmeron and P. J. Schuck, *Nat. Commun.*, 2015, **6**, 7993.

28 V. Carozo, Y. Wang, K. Fujisawa, B. R. Carvalho, A. McCreary, S. Feng, Z. Lin, C. Zhou, N. Perea-López, A. L. Elías, B. Kabius, V. H. Crespi and M. Terrones, *Sci. Adv.*, 2017, **3**, e1602813.

29 C. Kastl, R. J. Koch, C. T. Chen, J. Eichhorn, S. Ulstrup, A. Bostwick, C. Jozwiak, T. R. Kuykendall, N. J. Borys, F. M. Toma, S. Aloni, A. Weber-Bargioni, E. Rotenberg and A. M. Schwartzberg, *ACS Nano*, 2019, **13**, 1284–1291.

30 Q. Zhang, J. Lu, Z. Wang, Z. Dai, Y. Zhang, F. Huang, Q. Bao, W. Duan, M. S. Fuhrer and C. Zheng, *Adv. Opt. Mater.*, 2018, **6**, 1701347.

31 H. Gu, L. Chen, Y. Lu, F. Tian, Z. Zhang, K. Xu, J. Wu, V. D. Botcha, K. Li and X. Liu, *Jpn. J. Appl. Phys.*, 2018, **57**, 060309.

32 H. J. Conley, B. Wang, J. I. Ziegler, R. F. J. Haglund, S. T. Pantelides and K. I. Bolotin, *Nano Lett.*, 2013, **13**, 3626–3630.

33 Z. Liu, M. Amani, S. Najmaei, Q. Xu, X. Zou, W. Zhou, T. Yu, C. Qiu, A. G. Birdwell, F. J. Crowne, R. Vajtai, B. I. Yakobson, Z. Xia, M. Dubey, P. M. Ajayan and J. Lou, *Nat. Commun.*, 2014, **5**, 5246.

34 F. Wang, S. Li, M. A. Bissett, I. A. Kinloch, Z. Li and R. J. Young, *2D Mater.*, 2020, **7**, 045022.

35 A. Michail, D. Anestopoulos, N. Delikoukos, S. Grammatikopoulos, S. A. Tsirkas, N. N. Lathiotakis, O. Frank, K. Filintoglou, J. Parthenios and K. Papagelis, *J. Phys. Chem. C*, 2023, **127**, 3506–3515.

36 T. Lee, K.-Y. Lee, Y.-J. Lee, C.-H. Cho and H. Rho, *Curr. Appl. Phys.*, 2023, **49**, 115–119.

37 S. Roy, X. Yang and J. Gao, *Sci. Rep.*, 2024, **14**, 3860.

38 B. Zhu, X. Chen and X. Cui, *Sci. Rep.*, 2015, **5**, 9218.

39 J. Shang, X. Shen, C. Cong, N. Peimyoo, B. Cao, M. Eginligil and T. Yu, *ACS Nano*, 2015, **9**, 647–655.

40 K. Guan, Y. Li, L. Liu, F. Sun, Y. Wang, Z. Zheng, W. Zhou, C. Zhang, Z. Cai, X. Wang, S. Feng and T. Zhang, *Microsyst. Nanoeng.*, 2024, **10**, 132.

41 H. Y. Jeong, Y. Jin, S. J. Yun, J. Zhao, J. Baik, D. H. Keum, H. S. Lee and Y. H. Lee, *Adv. Mater.*, 2017, **29**, 1605043.

42 Y.-C. Lin, S. Li, H.-P. Komsa, L.-J. Chang, A. V. Krasheninnikov, G. Eda and K. Suenaga, *Adv. Funct. Mater.*, 2018, **28**, 1704210.

43 W.-H. Lin, W.-S. Tseng, C. M. Went, M. L. Teague, G. R. Rossman, H. A. Atwater and N.-C. Yeh, *ACS Nano*, 2020, **14**, 1350–1359.

44 G. H. An, S. J. Yun, Y. H. Lee and H. S. Lee, *Small*, 2020, **16**, 2003326.

45 C. Lee, B. G. Jeong, S. H. Kim, D. H. Kim, S. J. Yun, W. Choi, S.-J. An, D. Lee, Y.-M. Kim, K. K. Kim, S. M. Lee and M. S. Jeong, *npj 2D Mater. Appl.*, 2022, **6**, 67.

46 X. Wang, J. Dan, Z. Hu, J. F. Leong, Q. Zhang, Z. Qin, S. Li, J. Lu, S. J. Pennycook, W. Sun and C. H. Sow, *Chem. Mater.*, 2019, **31**, 7970–7978.

47 F. Cuccureddu, S. Murphy, I. Shvets, M. Porcu, H. Zandbergen, N. Sidorov and S. Bozhko, *Surf. Sci.*, 2010, **604**, 1294–1299.

48 R. Wang, D. Guo, G. Xie and G. Pan, *Sci. Rep.*, 2016, **6**, 29964.

49 Z. Zhang, P. Chen, X. Yang, Y. Liu, H. Ma, J. Li, B. Zhao, J. Luo, X. Duan and X. Duan, *Natl. Sci. Rev.*, 2020, **7**, 737–744.

50 S. Zhou, L. Liu, S. Cui, X. Ping, D. Hu and L. Jiao, *Nano Res.*, 2021, **14**, 1659–1662.

51 V. Voronenkov, B. Groven, H. Medina Silva, P. Morin and S. De Gendt, *Phys. Status Solidi A*, 2024, **221**, 2300943.

52 Y. Xia, X. Chen, J. Wei, S. Wang, S. Chen, S. Wu, M. Ji, Z. Sun, Z. Xu, W. Bao and P. Zhou, *Nat. Mater.*, 2023, **22**, 1324–1331.

53 A. Candeo, B. E. Nogueira de Faria, M. Erreni, G. Valentini, A. Bassi, A. M. de Paula, G. Cerullo and C. Manzoni, *APL Photonics*, 2019, **4**, 120802.

54 A. Genco, C. Cruciano, M. Corti, K. E. McGhee, B. Ardini, L. Sortino, L. Hüttenhofer, T. Virgili, D. G. Lidzey, S. A. Maier, A. Bassi, G. Valentini, G. Cerullo and C. Manzoni, *ACS Photonics*, 2022, **9**, 3563–3572.

55 D. Brida, C. Manzoni and G. Cerullo, *Opt. Lett.*, 2012, **37**, 3027–3029.

56 C. Trovatello, X. Zhu, A. Genco, G. Valentini, C. Cruciano, G. Cerullo, B. Ardini and C. Manzoni, *Opt. Mater.: X*, 2022, **14**, 100145.